nature photonics

Supplementary information

https://doi.org/10.1038/s41566-024-01480-5

Suppressed ion migration for high-performance X-ray detectors based on atmosphere-controlled EFG-grown perovskite $CsPbBr_3$ single crystals

In the format provided by the authors and unedited

Table of contents

This supplementary information file contains Supplementary Notes 1-17, Supplementary Figures 1-43, and Supplementary Table 1-9.

Supplementary Note 1. Comparison of the X-ray performance of semiconductor detectors

Supplementary Table 1. Comparison of the performance of semiconductor X-ray detectors.

Device structure	X-ray source (keV)	Electric field (V cm^{-1})	Sensitivity (μC Gy_{air}^{-1} cm^{-2})	Detection limit (nGy_{air} s^{-1})	Ref.
Au/$CsPbI_3$ QDs/Au	2.5	50000	1450	-	1
Cr/$MAPbBr_{2.94}Cl_{0.06}$ SC/C_{60}/BCP/Cr	8	600	8.4×10^5	7.6	2
α-Se	20	10000	20	5500	3
Au/Cs_4PbI_6 SC/Au	30	30	451.49	90	4
Au/$Rb_3Bi_2I_9$ SC/Au	30	3000	159.7	8.32	5
Au/$MA_3Bi_2I_9$-PPs/Au	35.5	2100	563	9.3	6
Au/BCP/C_{60}/$FA_{0.85}MA_{0.1}Cs_{0.05}PbI_3$ SC/Spiro TTB/Au	40	600	3.5×10^6	42	7
Au/$MAPbI_3$ SC/Au	50	1000	7×10^5	1.5	8
Au/$CsPbI_3$ SC/Au	50	41.7	2370	219	9
Bi/$CsPbBr_3$ SC/Au	50	~2100	>8000	<200	10
Au/$Cs_{0.1}FA_{0.85}GA_{0.05}Pb(I_{0.9}Br_{0.1})_3$ SC/Au	60	400	2.5×10^6	7.09	11
Ga/$CsPbBr_3$ film/Au	70	1200	1450	500	12
Au/$MAPbI_3$ SC/Au	100	33	1471.7	4.6×10^4	13
Au/$Cs_3Bi_2I_8Br$ SC/Au	100	4000	13000	28.6	14
ITO/Si-TFT/PI-$MAPbI_3$/$MAPbI_3$/PI-$MAPbBr_3$/ITO	100	2400	11000	-	15
Au/$MA_3Bi_2I_9$ SC/Au	100	60	10620	0.62	16
Au/CZT SC/Au	120	5000	6069	145	17
Cr/$MAPbBr_3$ SC/Au	120	150	1274	560	18
Cr/BCP/C_{60}/$(F\text{-}PEA)_2PbI_4$ SC/Au	120	1	3402	23	19
EGaIn/$CsPbBr_3$ SC/Au	120	5000	46180	10.81	This work

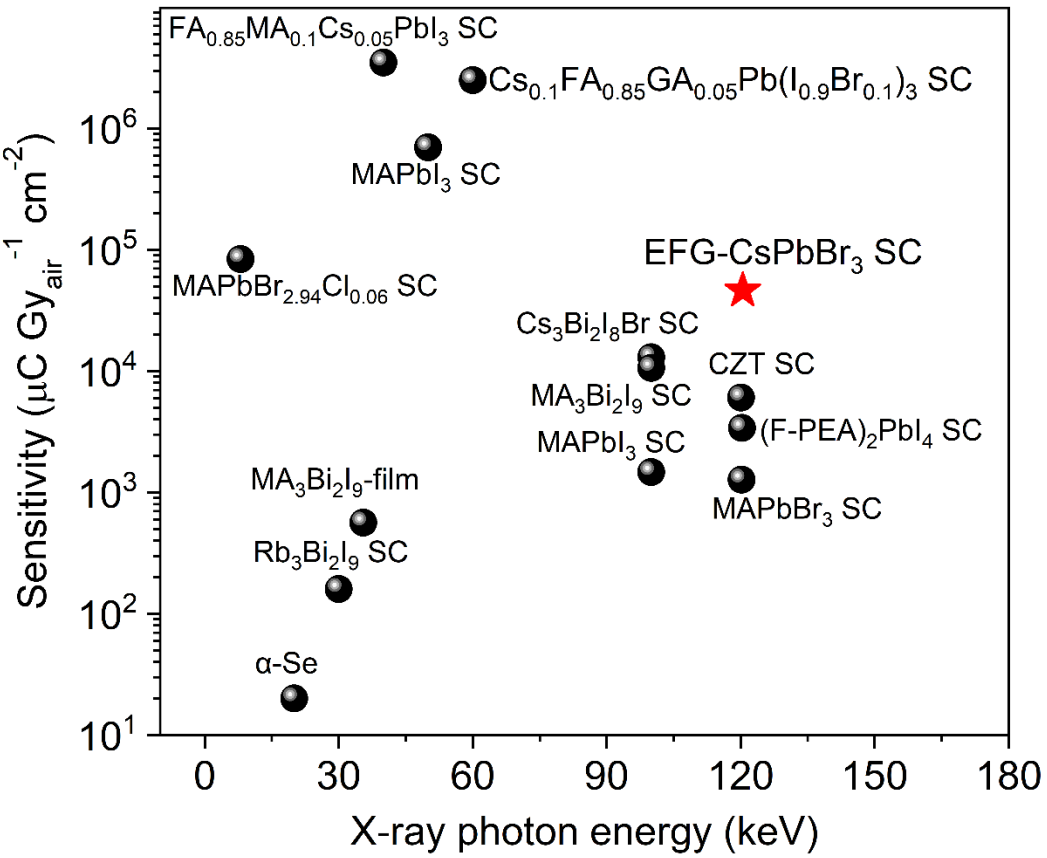

Supplementary Fig. 1. Comparison of the X-ray sensitivity under different X-ray energies of some semiconductor detectors and perovskites.

Supplementary Note 2: $CsPbBr_3$ SC growth by VB method

Supplementary Fig. 2a shows the photograph of the vertical Bridgman (VB) furnace. The high-purity CsBr (99.99%) and $PbBr_2$ (99.99%) raw materials with a stoichiometric ratio were sealed in the quartz tube in a vacuum at 600 °C for 24 h to form polycrystalline $CsPbBr_3$. The polycrystalline $CsPbBr_3$ was further purified with directional crystallization in the refined zone. The pure polycrystalline was then sealed into a quartz ampoule and moved to the 2-zone Bridgman furnace for $CsPbBr_3$ single-crystal growth. The high-temperature zone was 600 °C and the low-temperature zone was 200 °C, forming a temperature gradient of 10-15 °C cm^{-1}. The ampoule descended slowly with a speed of 1 mm h^{-1} which is beneficial to crystallization. After finishing growth, the temperature of the furnace cooled down to room temperature for 3 days, and the large-size and crack-free $CsPbBr_3$ single crystal was obtained by the VB method (Supplementary Fig. 2b). The crystals grown by the VB method are restricted by the sizes and shapes of ampoules.

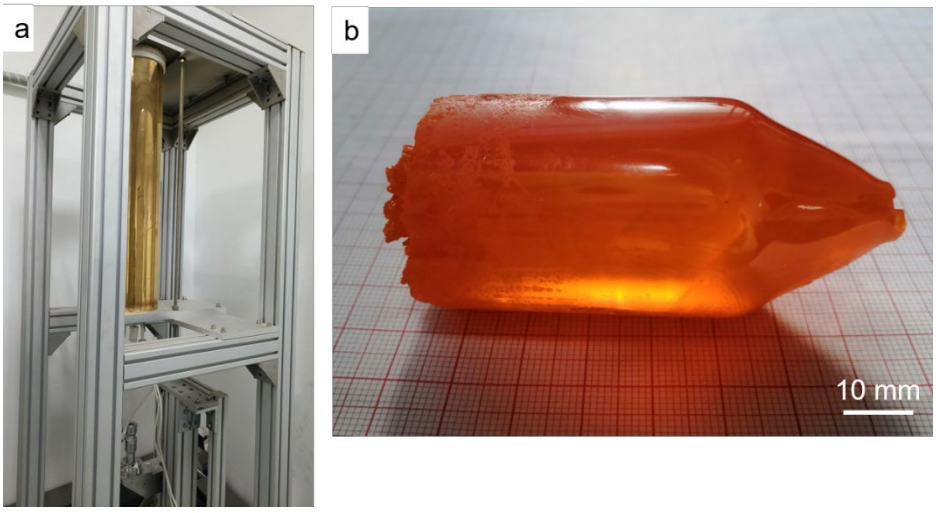

Supplementary Fig. 2 a) Photograph of the VB growth furnace. b) $CsPbBr_3$ single crystal grown by the VB method.

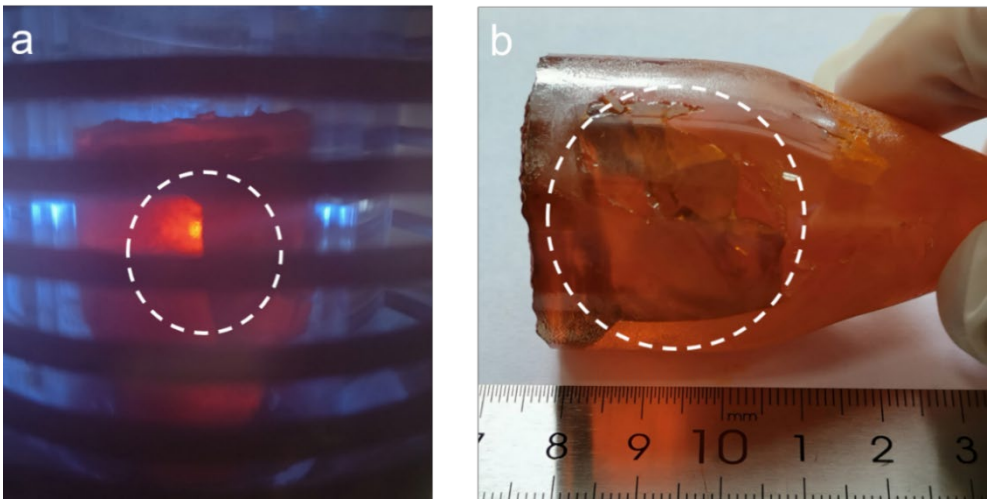

Supplementary Fig. 3 Photographs of a) VB-$CsPbBr_3$ SC in the cooling process, and b) as-grown VB-$CsPbBr_3$ SC with cracks.

Supplementary Note 3: $CsPbBr_3$ SC growth by EFG method

The edge-defined film-fed growth (EFG) method has been widely applied in the growth of sapphire[20], Ga_2O_3[21], and binary halides[22] single crystals. This technique possesses several advantages: (1) Near-size growth can reduce the material loss during the slicing and polishing process; (2) High growth rates of 5-10 mm h^{-1} increase the growth efficiency and reduce production costs; (3) Growth atmosphere can be regulated to compensate for the imbalance of volatiles. The shape of single crystals grown by the EFG method depends on the dies in the crucible, rather than the size of the crucibles. As shown in Supplementary Fig. 4a, the EFG furnace is composed of a quartz growth chamber, a heating system, a temperature measurement control system, a pulling system, a gas delivery system, a pull rod system, a thermal insulation system, and a growth crucible. The nominal wall thickness of the quartz tube was 5 mm to prevent the tube from bursting. The thermocouple was attached to the bottom of the quartz cavity. After the cavity was sealed, the air in the furnace was exhausted through the outlet, and the gas (Ar and HBr) was fed through the inlet.

In the EFG growth process, the synthesized $CsPbBr_3$ polycrystals were loaded on the growth crucible equably which was at the bottom of the quartz chamber. After the furnace was sealed completely, the whole system was evacuated to 10^1-10^2 Pa. The evacuated growth chamber was washed with Ar gas 3 times to remove the residual gas air further. Fifty millilitres of liquid HBr were poured into a glass bottle (volume: 500 mL; height: 160 mm; the radius of the neck: 45 mm; the radius of the bottom: 45 mm). Due to the boiling point difference of HBr (206 K) and H_2O (373 K), gaseous HBr with purified Ar gas would fill the whole furnace at 323 K. The furnace was heated to ~630 K in an Ar and HBr mixed atmosphere.

The highest temperatures inside the furnace decreased from 580 to 520 °C and the temperature gradient increased from 8 to 15 °C cm^{-1} as the pressure increased from -100 to 50 kPa because of the restrain of the heat convection with the heavy Ar and HBr atoms (Supplementary Fig. 4b). Supplementary Figs. 5, 6 illustrated the evolution of

the growth at different stages for cylindrical and tabular $CsPbBr_3$ crystals, respectively. The initial stage is the diameter expansion of the seed until it reaches the full die, then the crystal grows equably whose diameter keeps with the die diameter until growth termination in the advanced growth stage. Once the amount of remaining melt became less, the crystal was pulled up to avoid contact with the die. Owing to the large temperature gradient of the EFG furnace, a high growth speed of 5-10 mm h^{-1} was achieved, which is much faster than that of the VB method. After the crystal growth was completed, the temperature was cooled to room temperature for 72 h.

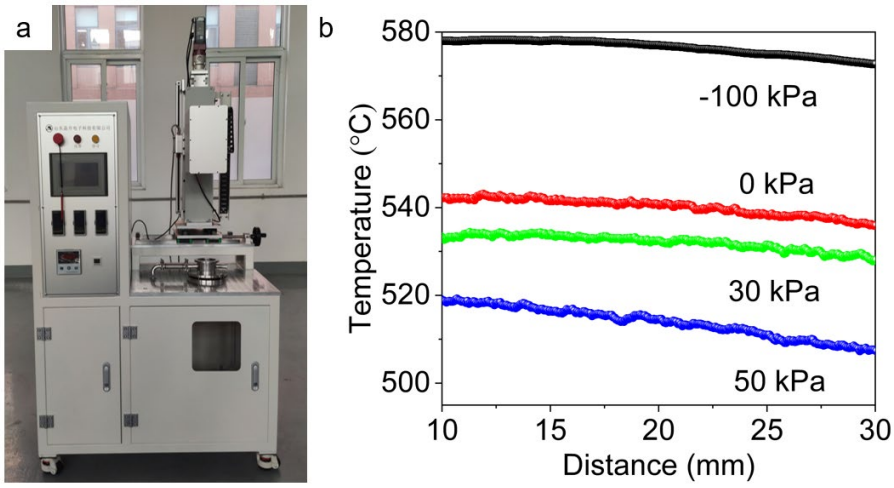

Supplementary Fig. 4 a) EFG growth furnace, and b) the axial thermal profiles at different pressure atmospheres as the temperature was set at 630 °C.

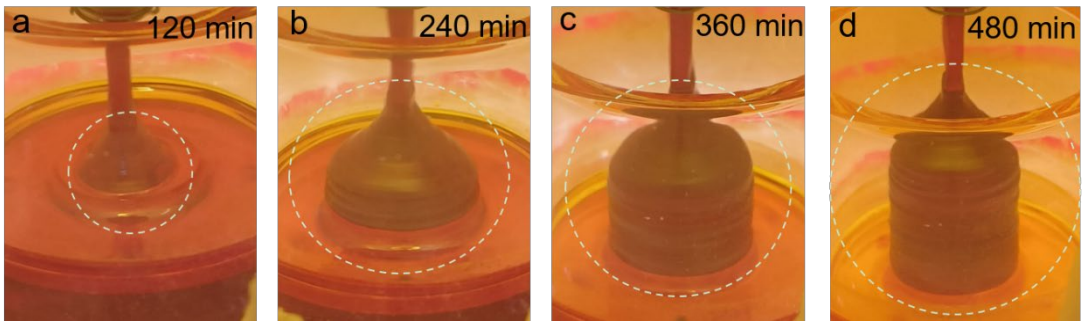

Supplementary Fig. 5 Evolution of the EFG growth at different stages for the cylindrical $CsPbBr_3$ crystal. a) diameter expansion during initial growth at 2 hours after seeding, b) reaching full die diameter at 5 hours after seeding, c) advanced growth stage at 6 hours after seeding, and d) final stage at 8 hours after seeding.

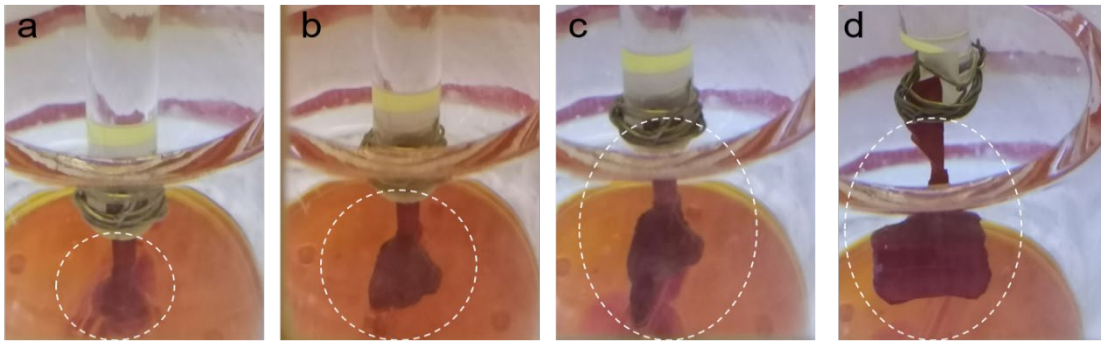

Supplementary Fig. 6 Evolution of the EFG growth at different stages for the rectangular $CsPbBr_3$ crystal. a) diameter expansion during initial growth, b) reaching full die size, c) advanced growth stage, and d) final stage.

Supplementary Fig. 7 EFG-$CsPbBr_3$ SC grown in the pure Ar atmosphere.

Supplementary Note 4. Photophysical characterization of $CsPbBr_3$ SCs

The surface reflection of a transparent media mainly refers to the refractive index *n* of the material. The reflectivity *R* can be calculated according to the Fresnel reflection formula[23]:

$$R=(n-1)^2/(n+1)^2 \quad (1)$$

where *n* is the refractive index of the crystals. If the light perpendicularly irradiates to the surface of a media, and ignoring the scattering and absorption, the maximum transmittance through two surfaces of the media can be calculated by[23]:

$$T=(1-R)^2=16n^2/(n+1)^4 \quad (2)$$

The reported refractive index of $CsPbBr_3$ is ~1.92[24]. Therefore, ignoring the absorption and scattering in the crystal, the theoretical maximum transmittance of $CsPbBr_3$ can be calculated as 81.1% based on the above equation 2.

However, scattering and absorption often exist in the real crystals, which deteriorates the transmittance of the crystals. The scattering mainly arises from the volume defects such as the inclusions and second phases, and the absorption mainly arises from the point defects or impurities. They are both affected by the thickness of the crystals. Based on the above conception, we carefully examined our experiment procedures in the sample preparation and transmittance measurement. The size of the single crystal wafers was carefully controlled in the same cutting and polishing process to ensure consistency in the measurement, and the aperture of the wafers is 4.0 × 4.0 mm^2, and the thickness of the wafers is 2.01 mm. Though the transmittance of the crystal has been greatly improved by improving the VB growth parameters for restraining the inclusions, a small number of remaining inclusions in some VB-$CsPbBr_3$ crystals will still deteriorate the transmittance (77%). In comparison, the EFG-$CsPbBr_3$ grown in the Ar-HBr atmosphere with high optical transparency (80%) can prevent the formation of inclusions, and the crystals almost reach the theoretical maximum transmittance.

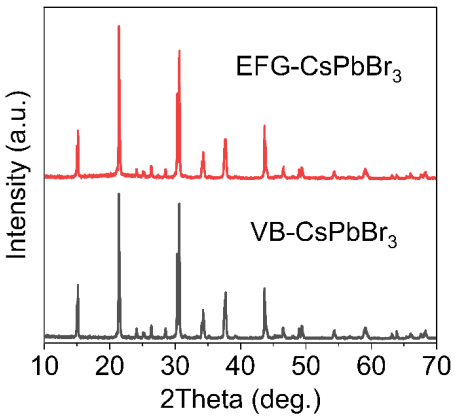

Supplementary Fig. 8 PXRD patterns of the EFG- and VB- $CsPbBr_3$ SCs.

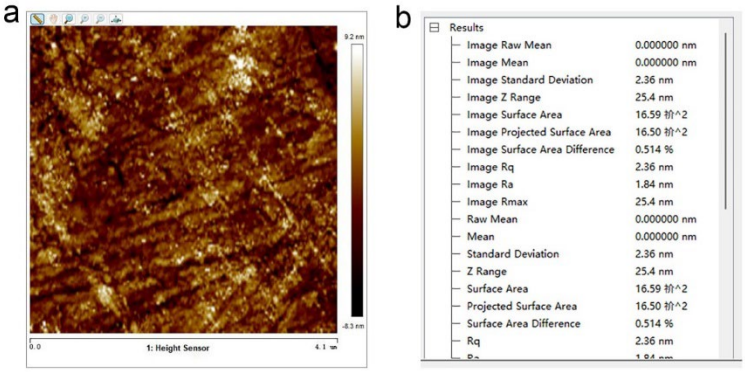

Supplementary Fig. 9 a) AFM image of the polished surface. b) Roughness of the polished surface of the $CsPbBr_3$ crystal wafer. The average surface roughness was < 2 nm.

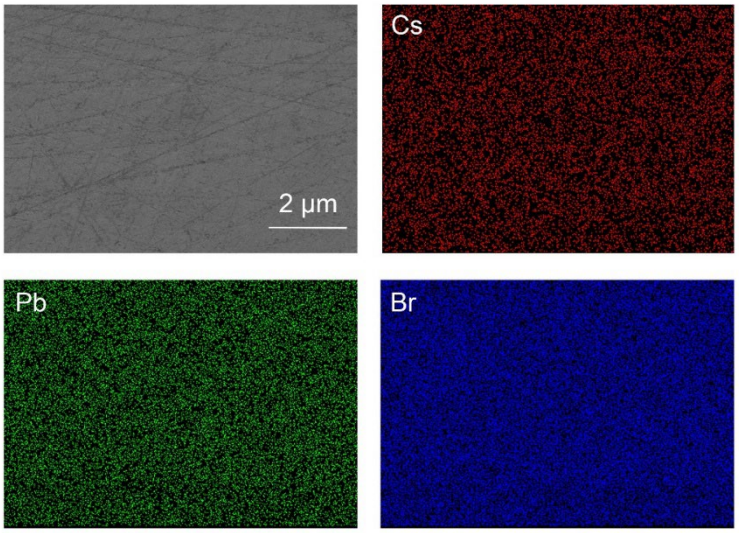

Supplementary Fig. 10 SEM image and EDS mapping of the Cs, Pb, and Br elemental distribution of EFG-$CsPbBr_3$ SC.

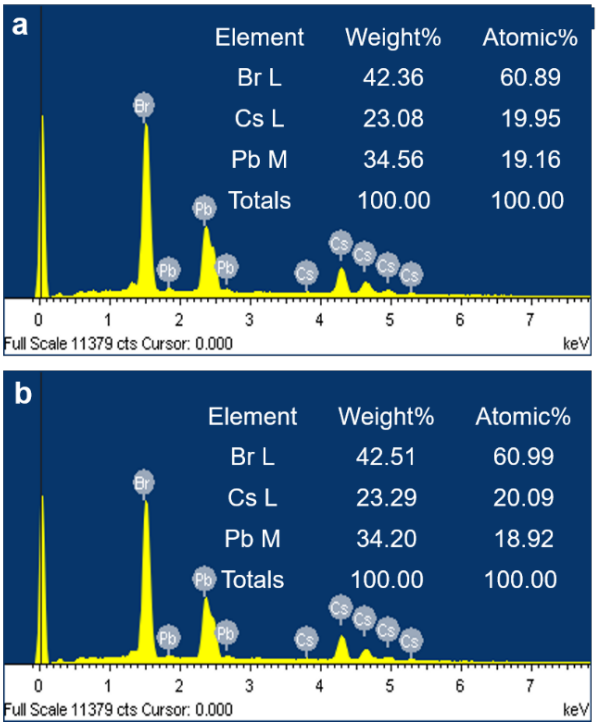

Supplementary Fig. 11 EDS spectra of a) VB- and b) EFG-$CsPbBr_3$ SCs.

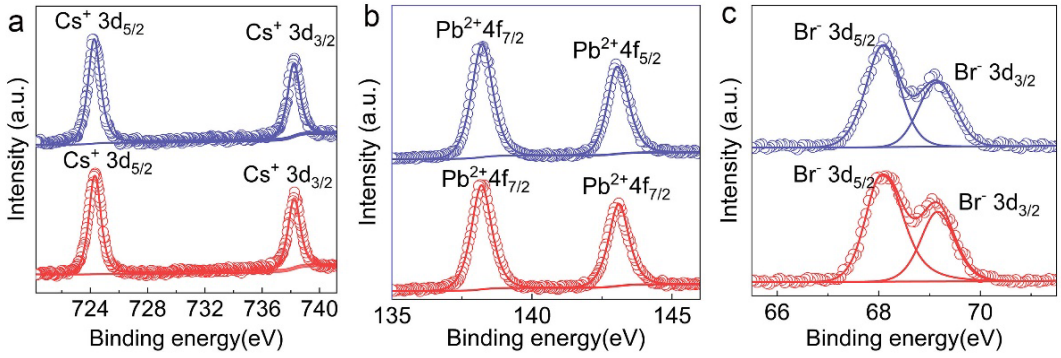

Supplementary Fig. 12 XPS spectra of Cs 3d, Pb 4f, and Br 3d for EFG- (blue) and VB- (red) $CsPbBr_3$ SCs. Separated spin-orbital components were found at 13.96, 4.83, and 1.06 eV, conforming to the +1, +2, and -1 oxidation states for Cs, Pb, and Br, respectively. The results demonstrate that impurities are hardly formed in EFG-$CsPbBr_3$ SC.

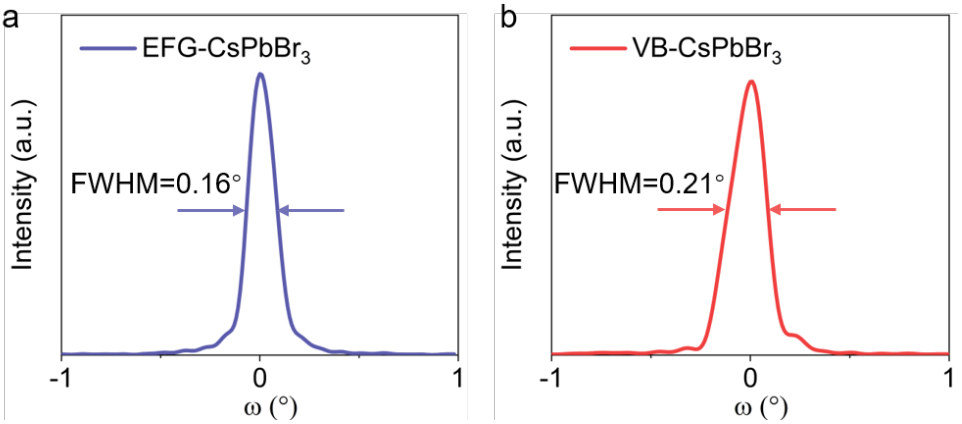

Supplementary Fig. 13 X-rays rocking curves of the EFG- and VB- $CsPbBr_3$ SCs.

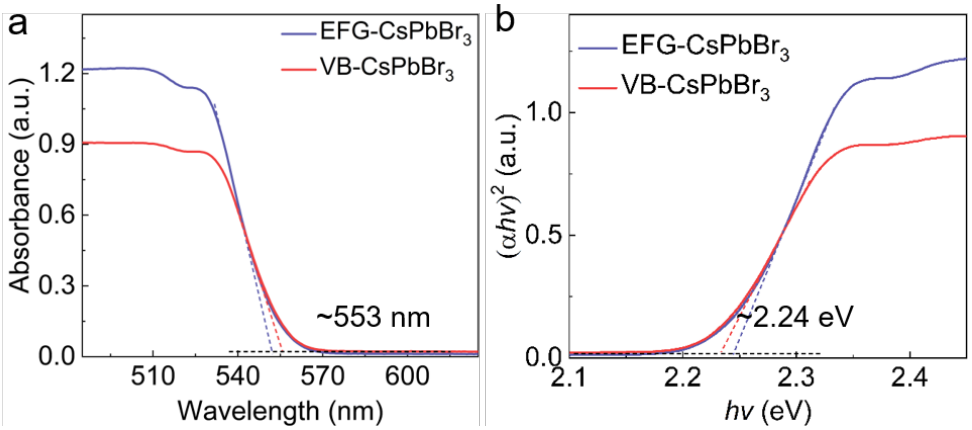

Supplementary Fig. 14 a) Ultraviolet−visible absorption spectra and b) Tauc plot curves of the EFG- and the VB- $CsPbBr_3$ SCs.

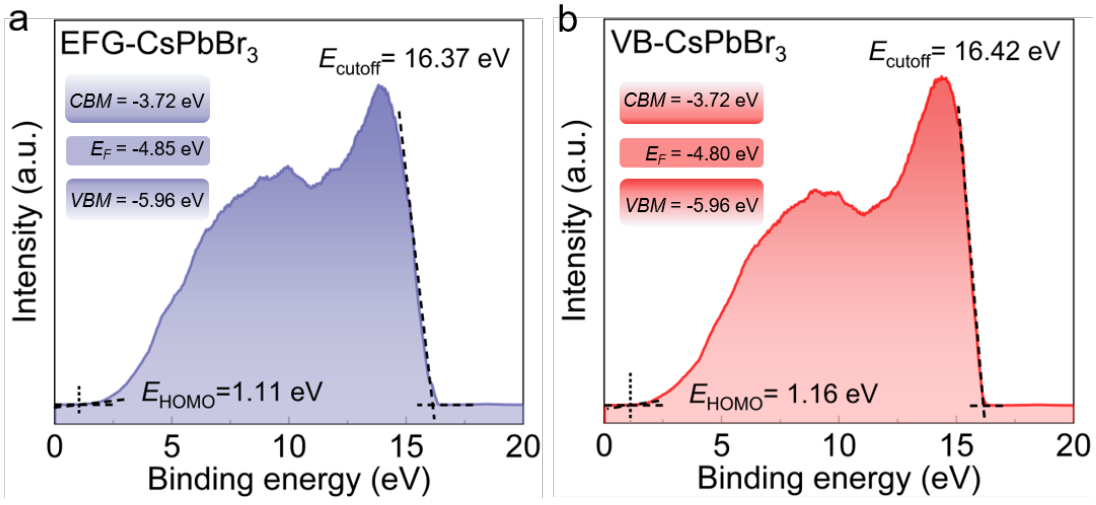

Supplementary Fig. 15 Ultraviolet photoelectron spectra of the $CsPbBr_3$ SCs. The Fermi level (E_F), valence band maximum (E_v), and conduction band minimum (E_C) were calculated based on the cut-off binding energies ($E_{cut\text{-}off}$), bandgaps, and Fermi edges (E_{HOMO}).

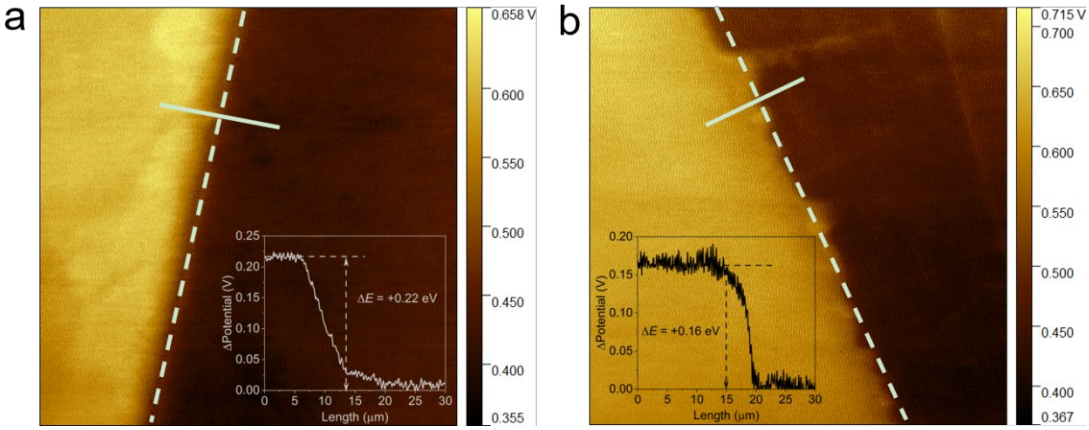

Supplementary Fig. 16 KPFM potential images with Au work function as a reference between an Au electrode and the SC for a) VB-$CsPbBr_3$ SC and b) EFG-$CsPbBr_3$ SC. Insets to a and b show the corresponding potential profiles along the white solid lines, showing that ΔE_F are 0.16 and 0.22 eV for EFG-$CsPbBr_3$ and VB-$CsPbBr_3$, respectively. The Fermi level of EFG-$CsPbBr_3$ SC is 0.06 eV smaller than that of VB-$CsPbBr_3$ SC, which is beyond the error of 0.01 eV for the KPFM measurements. The crystal wafers were fine polished, and an 80 nm-thickness Au film was evaporated on the surface of the crystal as a reference.

Supplementary Note 5: Carrier transport properties measured by time of flight (ToF) method

5.1 Mobility-lifetime product ($\mu\tau$)

Non-collimated ^{241}Am α-particles with an energy of 5.48 MeV were used as the radiation source to test the radiation detection performance of the crystal at room temperature. Since α particles only penetrate within a few microns below the surface of the material, which are negligible compared to the thicknesses of the crystal (1.35 mm), it could be considered that large numbers of electron-hole pairs are generated near the surface. As shown in Supplementary Fig. 17, the prepared detector was placed in a closed shielded box connected to an eV-550 preamplifier. High-energy particles are incident on the crystal surface (^{241}Am radiation source is 3 cm away from the wafer surface), ionizing the crystal to generate a large number of electron-hole pairs. Under the action of an external electric field, the electrons and holes move toward the anode and cathode respectively. The signal of the preamplifier is further amplified and shaped by an ORTEC amplifier (model 570) with a gain of 0.5~200 and a shaping time of 1~10 μs. Finally, the signal is evaluated by inputting it into an 8K multi-channel analyzer (model ORTEC EASY-MCA-8K), and read into the EASY-MCA-8K software to generate an energy spectrum response spectrum. Combined with the single-carrier Hecht equation fitting, the carrier mobility and lifetime product of the material are calculated.

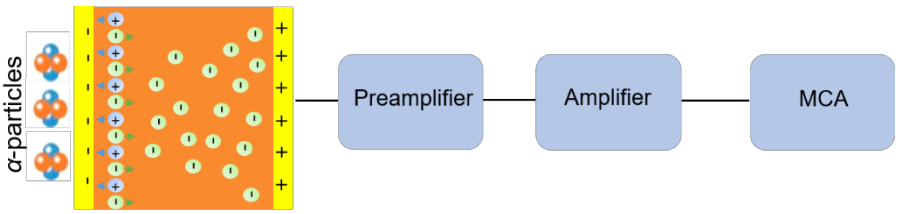

Supplementary Fig. 17 Diagram of the carrier transport process irradiated by α-particles.

The $\mu\tau$ values of the Au/SC/Au devices were extracted by the voltage dependence of the channel value with the modified Hecht equation[25]:

$$\frac{Q}{Q_0} = \frac{\mu\tau U}{d^2}\left(1 - \exp\left(-\frac{d^2}{\mu\tau U}\right)\right) \quad (3)$$

where Q is the channel value of the all-energy peak, Q_0 is the saturation channel value of each peak, U is the applied bias voltage, and d is the sample thickness. The thicknesses of the EFG-$CsPbBr_3$ single crystal and the VB-$CsPbBr_3$ single crystal are 1.35 mm. Au electrodes were sputtered on both sides of the wafers, and the areas of the electrodes were 2.0 × 2.0 mm^2. The Au/EFG-$CsPbBr_3$/Au device exhibits lower noise signals and higher voltages than the Au/VB-$CsPbBr_3$/Au device because of the higher resistance of the EFG-$CsPbBr_3$ crystal.

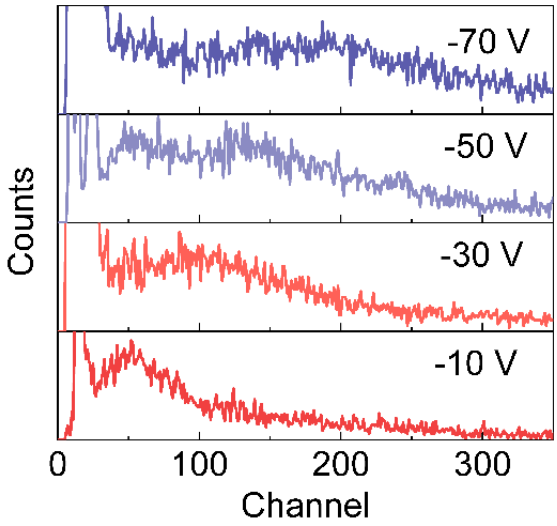

Supplementary Fig. 18 Energy-resolved spectrum of ^{241}Am α-particle with a characteristic energy of 5.48 MeV using a shaping time of 10 μs under negative voltages of Au/VB-$CsPbBr_3$ SC/Au device.

5.2 Mobility (μ)

The current pulse signal generated by the device is collected, amplified, and converted into a voltage pulse signal by the preamplifier. Then the signal is collected to obtain the carrier drift time (t), and the average fall time decreases with the increase of the bias voltage using an oscilloscope, and the time between 10% and 90% of the amplitude range is regarded as the carrier drift time of the pulse signal. To increase the

credibility of the data, we take 500 points for each voltage to carry out the data statistics of the transit time, and the statistical results are shown in Supplementary Figs. 19 and 21. We regard the fall time with the greatest probability of occurrence at each voltage as the transit time under that bias voltage (Fig. 2h and Supplementary Fig. 20). The carrier mobility μ was calculated using the equation[26]:

$$\mu = \frac{v}{E} = \frac{d}{Ut} \tag{4}$$

where v is carrier drift velocity, E is the electric field, and d is the sample thickness.

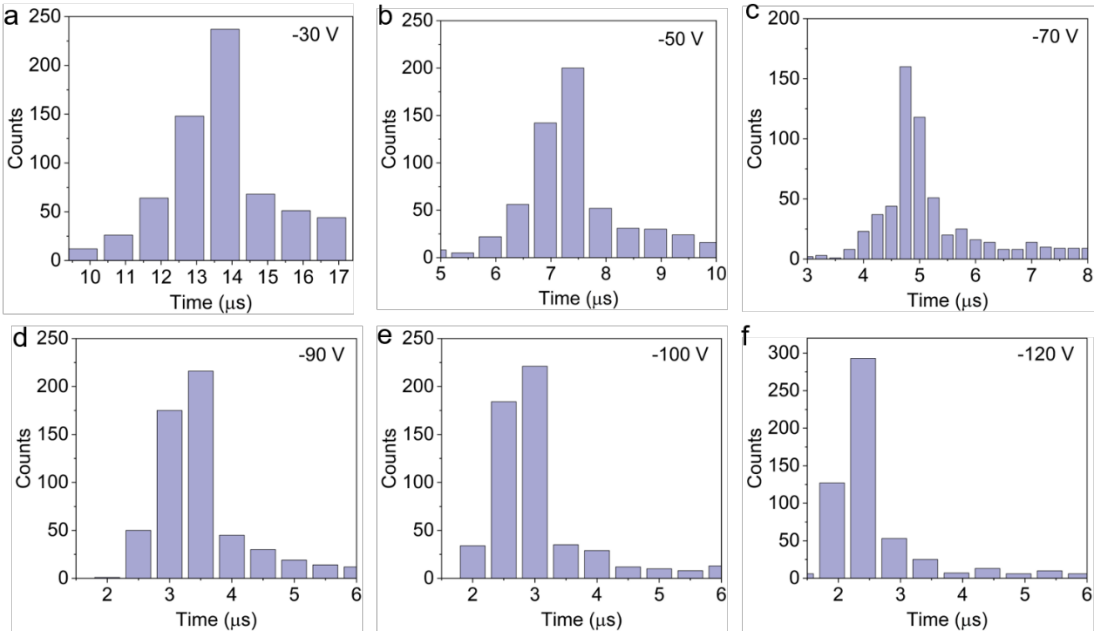

Supplementary Fig. 19 A histogram of rise time distribution under -30, -50, -70, -90, -100, and -120 V for the Au/EFG-$CsPbBr_3$ SC/Au device.

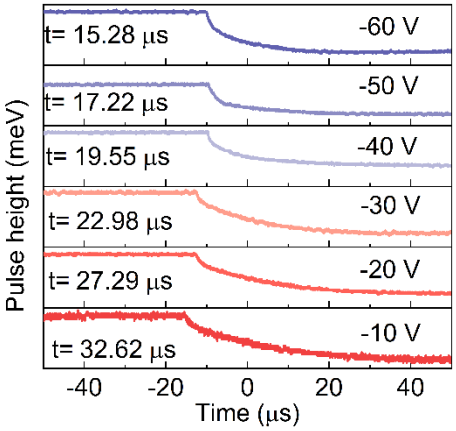

Supplementary Fig. 20 Induced α-pulse shapes at different negative voltages of Au/VB-$CsPbBr_3$ SC/Au device.

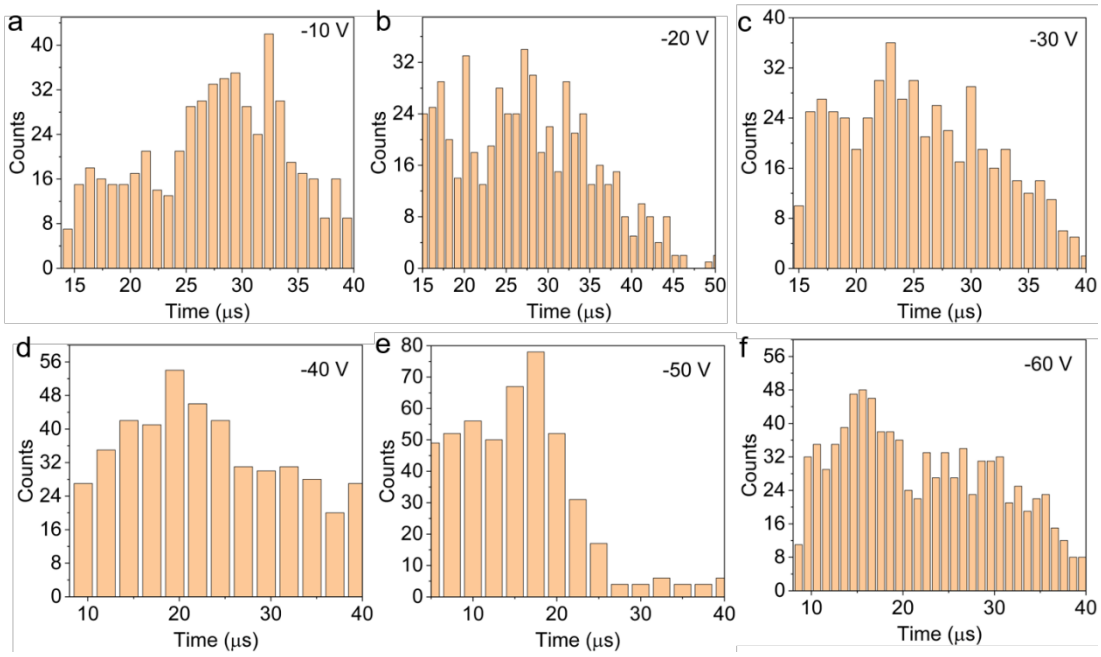

Supplementary Fig. 21 A histogram of rise time distribution under -10, -20, -30, -40, -50, and -60 V for Au/VB-$CsPbBr_3$/Au device.

Supplementary Note 6: Current-voltage curves of $CsPbBr_3$ SCs

The electric properties of EFG- and VB-$CsPbBr_3$ SCs were studied with Au/SC/Au devices. The *I-V* curves were measured under dark conditions, and the resistivities were calculated in the bias range of -1 to 1 V. The thicknesses of the samples are near 1.10 mm, and the Au electrodes coated on both planes of the samples were all 2.0 × 2.0 mm^2. The current-voltage loops were measured under dark and the scan rates were 1, 2, 4, and 10 V s^{-1}.

Similar to the growth of $CsPbBr_3$ SCs using the VB method, we found that the $CsPbBr_3$ SC grown in pure Ar produced large dark currents (-10 ~ -50 nA @-100V) and obvious *I-V* hysteresis for Au/$CsPbBr_3$ SC/Au device (Supplementary Fig. 24), indicating the strong ion migration properties. Therefore, the HBr-Ar atmosphere was regarded as one of the most important parameters in suppressing ion migration by the compensation of defects.

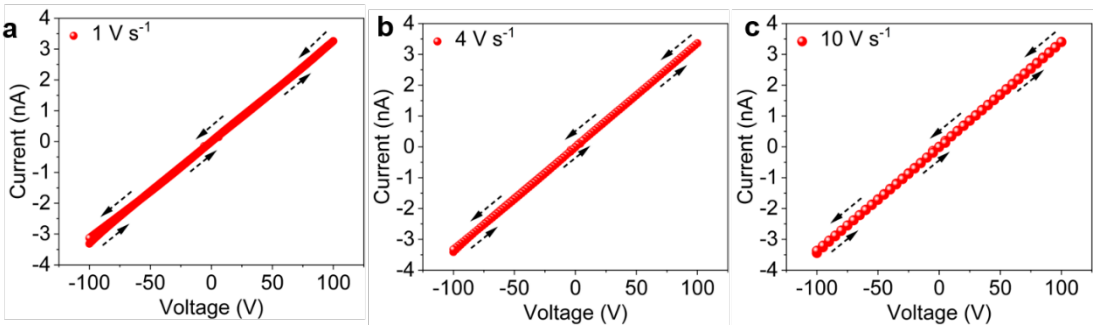

Supplementary Fig. 22 Current-voltage loops of Au/EFG-$CsPbBr_3$ SC/Au from -100 to 100 V at the scan rate of a) 1 V s^{-1}, b) 4 V s^{-1}, c) 10 V s^{-1}.

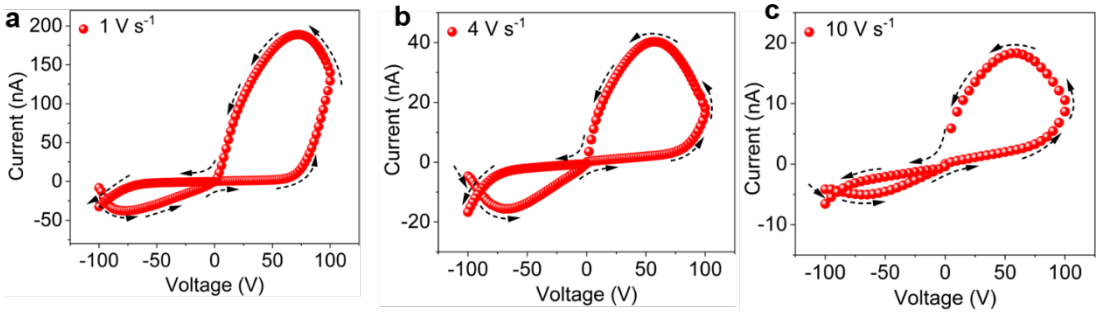

Supplementary Fig. 23 Current-voltage loops of Au/VB-$CsPbBr_3$SCs/Au from -100 to 100 V at the scan rate of a) 1 V s^{-1}, b) 4 V s^{-1}, c) 10 V s^{-1}.

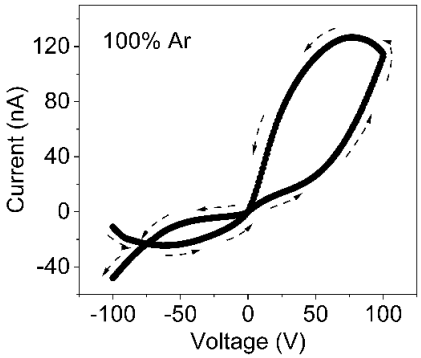

Supplementary Fig. 24 Current-voltage loops of Au/EFG-$CsPbBr_3$ SC for the pure Ar atmosphere/Au from -100 to 100 V at the scan rate of 2 V s^{-1}.

Supplementary Note 7: Space-charge-limited current (SCLC) measurements

SCLC measurements have been widely used to study the charge carrier mobility and trap density in semiconductors. Mott and Gurney proposed in 1941 that the space charge limits the current increment. When the applied voltage is gradually increased, that is, when excessive carriers are injected from the injection electrode into the medium with relatively low carrier mobility, part of the carriers will not flow from the lifting electrode to the external circuit but will reside in the medium, forming a space trap and hindering subsequent filling. The trap state densities were calculated as[27]:

$$n_{\text{trap}}=\frac{2\varepsilon\varepsilon_0 V_{\text{TEL}}}{eL^2} \tag{5}$$

where V_{TEL} denotes the trap-filling limit voltage, L denotes the thickness of the wafer, ε denotes the relative dielectric constant for $CsPbBr_3$, ε_0 is the vacuum permittivity, and e is the elementary charge. According to equation S5, the trap-filling limit voltage V_{TEL} is inversely proportional to the square of thickness L^2. Therefore, the thin plate sample facilitates obtaining the low trap-filling limit voltage.

However, perovskites are ion-electron hybrid semiconductors, i.e. the influence of ion migration in perovskites on the space-charge limited current measurement is significant. During the SCLC measurement with continuous voltages, the VB-$CsPbBr_3$ SC exhibited large hysteresis between the forward and reverse voltage scans (Supplementary Fig. 25b), indicating the strong movement of ions results in inaccurate SCLC analysis. In contrast, the EFG-$CsPbBr_3$ SC demonstrates minor hysteresis (Supplementary Fig. 25a), proving that the migration of ions is significantly suppressed. To minimize the different effects of ions migration on SCLC results, we used the Pulsed voltage Space-Charge-Limited Current (PV-SCLC) measurements for obtaining reliable *I-V* curves with suppressed hysteresis[28]. The test procedure is as follows, set t_{bvp} (time between voltage pulses, the time interval between two applications of pulse voltage) > $t_{\text{ion-diff}}$ (average ion diffusion time) so that the ions can return to their original position each time a pulse voltage is applied. Then an appropriate pulse voltage

integration time (which can both obtain space charge limited current and avoid ion interference) was used to obtain an accurate hysteresis-free SCLC measurement method. The hysteresis effect almost completely disappeared after measurement using the PV-SCLC method.[28] In our PV-SCLC measurements, we applied a thin plate sample of 900 μm thick to extend the Child regime. The size of the Au electrode is 3.0 mm × 3.0 mm × 30 nm for all samples, and the area of the Au electrode is 9.00 mm^2. We set t_{bvp}=10 min, and the bias voltage was set to 500 V.

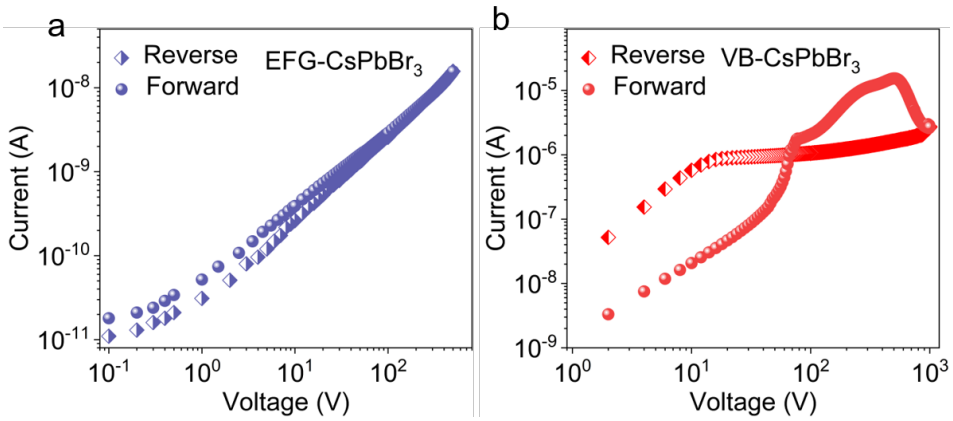

Supplementary Fig. 25 Large hysteresis between forward (bar points) and reverse (grid points) *I-V* curves during the SCLC measurement of a) EFG-$CsPbBr_3$ and b) VB-$CsPbBr_3$ single crystals with the continuously applied electric field.

Supplementary Note 8: Time-resolve microwave conductivity (TRMC) measurements

Time-resolved microwave conductivity (TRMC) is a noncontact technique that probes the photoconductivity of a material with microwaves and is excited with a wavelength and intensity tunable nanosecond laser. The TRMC setup mainly includes three parts: photoexcitation, microwave waveguide, and microwave detection. The nanosecond pump laser has a pulse energy of > 5 mJ, and it can be tuned easily with attenuation. The pulse width is ∼7 ns, which determines the time resolution. The perovskite SCs were placed within a brass cavity and excited with the nanosecond laser at various wavelengths of light. The reflected microwave power was highly dependent on the conductivity of the perovskite thin films, which is closely related to the charge carrier density and mobility given by

$$\sigma = qn\mu \tag{6}$$

where q is the elementary charge, n is the carrier density, and μ is the mobility. Hence, by probing the change in the reflected microwave power (ΔP), we can determine the change in conductivity as follows[29]

$$\Delta\sigma = -\Delta K\frac{\Delta \mathrm{P(t)}}{P} \tag{7}$$

where K is the correction factor and P is the incident microwave power. Having carefully calibrated the light intensity, we can calculate the excess carrier density, assuming excellent charge generation of the unit in perovskites.

To analyze the shallow-trap induced trapping and de-trapping processes, we also fitted the TRMC decays with continuous equations of the kinetic mode reported previously[29,30],

$$\frac{\mathrm{d}n_e}{\mathrm{d}t} = G_C - k_2 n_e n_h - k_T n_e (N_T - n_t)\ , \tag{8}$$

$$\frac{\mathrm{d}n_h}{\mathrm{d}t} = G_C - k_2 n_e n_h - k_R n_t n_h\ , \tag{9}$$

$$\frac{\mathrm{d}n_t}{\mathrm{d}t} = k_T n_e (N_T - n_t) - k_R n_t n_h\ , \tag{10}$$

where G is the generation rate of the photoexcitation, reflecting the number of electrons

excited from the valance band (VB) to conduction band (CB). k_2 is the bimolecular recombination rate constant, which is closely related to the radiative recombination. N_t represents the total density of trap states, k_t and k_r are the charge carrier trapping and depopulation rate constants. $n(t)$, $p(t)$ and $n_t(t)$ are the electron, hole, trapped electrons as a function of time. Then, the TRMC decay is a representative of the whole free carriers (electrons and holes) versus time. It should be noted that the carriers in our TRMC measurement were mainly generated on the surface of perovskite SCs as a result of the 532 nm laser being used as the excitation light. The shallow trap states obtained from this measurement may affected by the surface states, due to the high absorption coefficient and low penetration depth of visible photons in perovskite single crystals. In our measurement, the thicknesses of the samples are 1.0 mm and the square areas are 4.0×4.0 mm^2.

Supplementary Note 9: Ion migration properties with impedance spectroscopy (IS) measurements

IS measurements were carried out to investigate the carrier transport and ion migration process in $CsPbBr_3$ single crystal. The temperature-dependent Nyquist plots and the complex impedance part with the frequencies were measured in the dark using an electrochemical workstation (CHI, 660E) equipped with a frequency response analyzer. The geometric area of the SC samples was controlled to be 3.8 × 3.8 × 0.7 mm^3 (Supplementary Fig. 26). The thickness of samples for impedance spectroscopy measurement is 0.7 mm. Conductive silver glue is used to connect the Au/$CsPbBr_3$ SC/Au device to the copper wire to facilitate connection with the instrument, and the area of electrodes is 3.0 × 3.0 mm^2. The measurements were performed between 1 MHz and 0.1 Hz with an amplitude of 30 mV. The movement of ions can be accessible in the intermediate-frequency domain (100-800 Hz).[31,32]. The activation energy of the ionic diffusion was obtained by fitting the imaginary impedance and frequency at different temperatures (Supplementary Fig. 29) through the Arrhenius equation[32]:

$$\ln(f) = C - E_a / k_B T \quad (11)$$

where f denotes the escape frequency, C is a constant, E_a denotes the ion activation energy, k_B is the Boltzmann constant, and T is the absolute temperature.

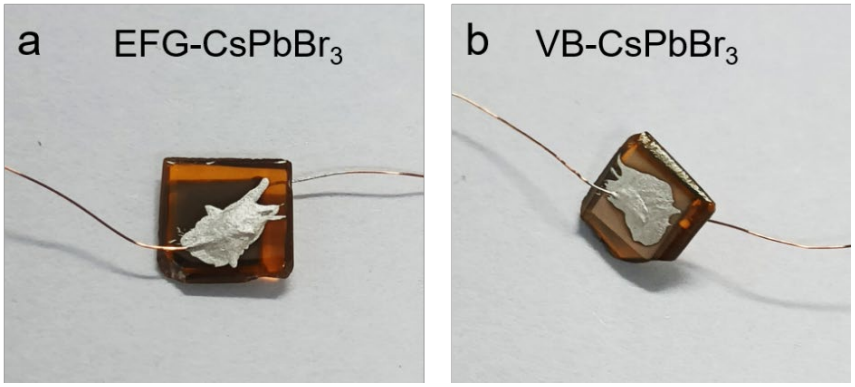

Supplementary Fig. 26 Samples for the EFG- and VB-$CsPbBr_3$ SCs. The thickness of samples for impedance spectroscopy measurement is 0.7 mm.

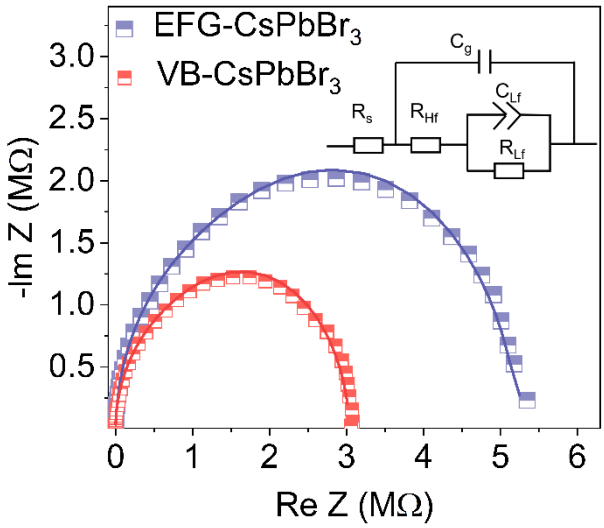

Supplementary Fig. 27 Nyquist plots of the EFG- and VB-$CsPbBr_3$ single crystals at 0.2 V DC bias in the frequencies ranging from 1 MHz to 1 Hz under dark at 298 K under dark. The inset is the equivalent circuit that is used to fit the IS data of the $CsPbBr_3$ SCs, in which R_s is series resistance, R_{HF}, and R_{LF} the high-, and low-frequency resistances, respectively. C_g is the geometric capacitance, C_{Lf} is the low-frequency capacitance[33]. The Nyquist plots of both devices were fitted according to the equivalent circuit model (the inset)[33], and the corresponding fitting parameters were obtained from the equivalent circuit model and listed in Supplementary Tables 2 and 3.

Supplementary Table 2 Parameters obtained from the fitted plots of the impedance spectra in the EFG-$CsPbBr_3$ device using an equivalent circuit model.

Temperature (K)	R_s (Ω)	R_{Hf} (Ω)	R_{Lf} (Ω)
298	515	2.68E6	2.58E6
308	423	2.38E6	1.53E6
318	395	1.64E6	1.35E6
328	357	9.51E5	7.75E5
338	336	4.44E5	2.48E5

Supplementary Table 3 Parameters obtained from the fitted plots of the impedance spectra in the VB-$CsPbBr_3$ devices using an equivalent circuit model.

Temperature (K)	R_s (Ω)	R_{Hf} (Ω)	R_{Lf} (Ω)
298	488	1.74E6	1.30E6
308	476	1.26E6	1.18E6
318	407	1.19E6	7.17E5
328	312	8.54E5	6.57E5
338	347	6.12E5	4.95E5

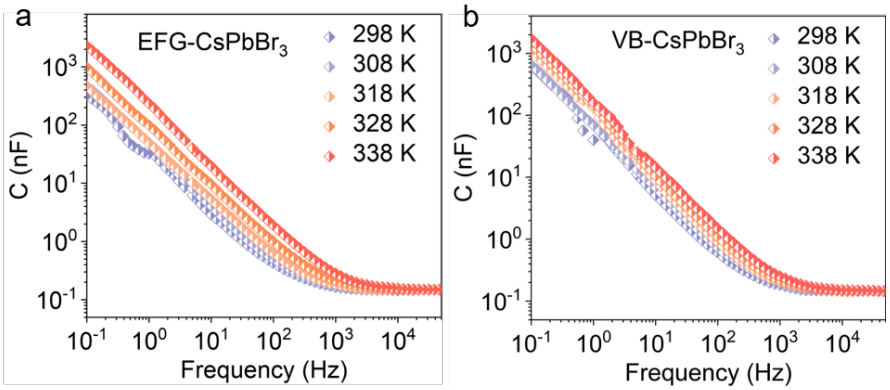

Supplementary Fig. 28 Capacitance spectra with the frequencies of a) EFG- $CsPbBr_3$ and b) VB-$CsPbBr_3$ crystals at the temperature from 298 to 338 K.

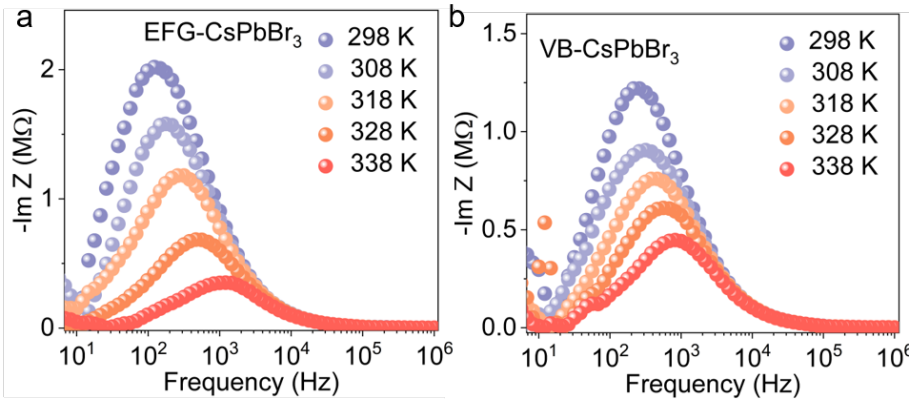

Supplementary Fig. 29 Complex impedance part with the frequencies of a) EFG-$CsPbBr_3$ and b) VB-$CsPbBr_3$ crystals at the temperature from 298 to 338 K.

Supplementary Note 10: Ion migration properties with temperature-dependent transient current response method

The temperature-dependent transient current response method was also adopted to compare the diffusion barriers. The typical charging-discharging process curve of the $CsPbBr_3$ SC is shown in Supplementary Fig. 30. An external bias was applied to the crystal to promote ionic diffusion until the ions reached equilibrium. Once the bias was removed, the ion vacancies migrated back to the opposite electrode due to the ion concentration grade, leading to an opposite current. The ion migration kinetics could be entirely manifested by the decay of the opposite current. Therefore, the activation energy of the ionic diffusion could be obtained by fitting the Arrhenius equation to the current-time curves obtained at different temperatures[3]:

$$\ln k = C - E_a / k_B T \quad (12)$$

where k denotes the decay rate, C is a constant, E_a denotes the ion activation energy, k_B is the Boltzmann constant, and T is the absolute temperature. The currents gradually increased due to the increased intrinsic carrier concentration of the $CsPbBr_3$ SC when the temperature was increased from 268 to 328 K (Supplementary Fig. 31). As shown in Supplementary Fig. 32, the ion activation energy of the EFG-$CsPbBr_3$ SC was 202.07 meV, much higher than that of the VB-$CsPbBr_3$ SC (122.07 meV) and ITC-$CsPbBr_3$ SC (160.0 meV), which confirmed that the ion migration of $CsPbBr_3$ SCs could be suppressed by atmosphere-controlled growth.

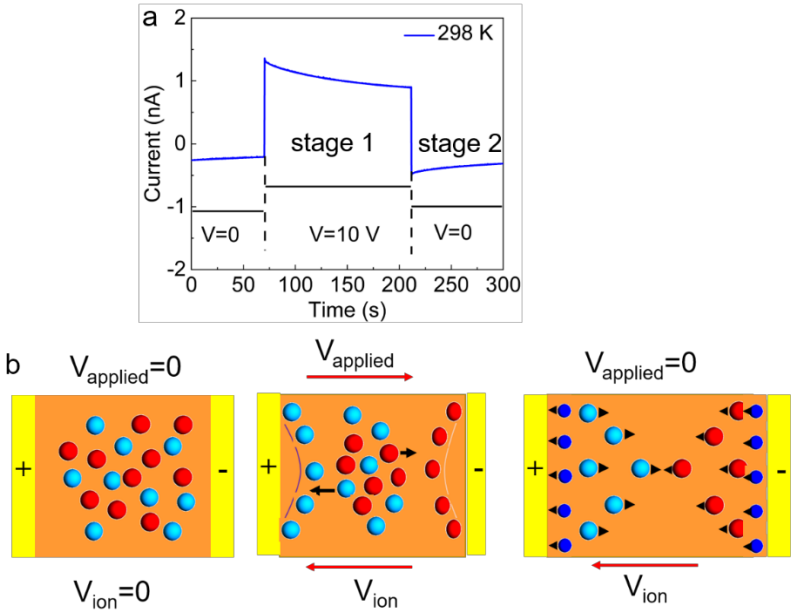

Supplementary Fig. 30 (a) Temporal response curves following positive and negative biasing at 298 K. The bias sequences are also displayed as solid lines as well. The applied external bias is 10 V. Stage 1: the external bias is applied, and stage 2: the external bias is removed. (b) Schematic diagrams indicating the dynamics of ionic transport following external bias.

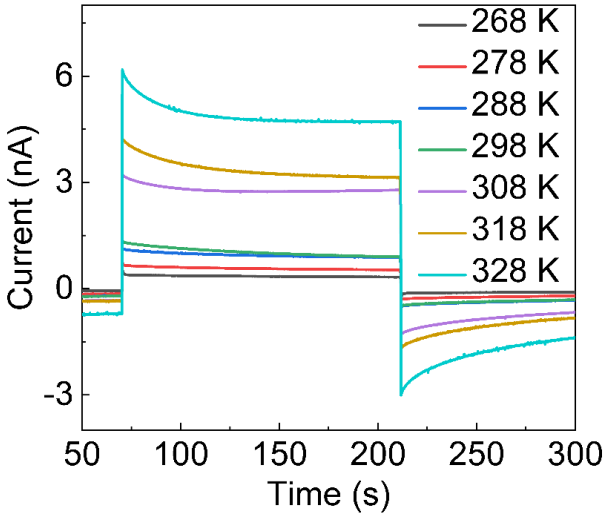

Supplementary Fig. 31 Typical charging-discharging process curves of $CsPbBr_3$ SC coplanar-structure device in the dark at a range of 268-328 K.

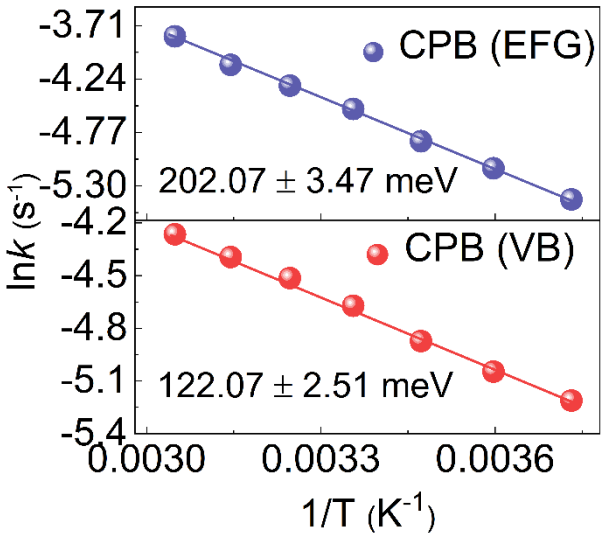

Supplementary Fig. 32 Ion migration activation energies of $CsPbBr_3$ SCs.

Supplementary Table 4 Summary of the defects in $CsPbBr_3$ crystals obtained from the TSC spectra.

Growth method	T_m (K)	E_a (eV)	Concentration(cm^{-3})	Point defect	References
Solution Method	64.3	0.104	2.06×10^{13}	Br_{Cs}^{2-}	34
	99.5	0.176	1.21×10^{14}	V_{Cs}^{-}	
	155.5	0.299	2.42×10^{13}	Pb_i^{2+}	
	228.9	0.471	1.78×10^{12}	Pb_{Br}^{2+}	
Solution Method	**67**	**0.106**	6.81×10^{15}	$\mathbf{V_{Br}^{+}}$	35
	115	0.204	2.07×10^{15}	Pb_i^{+}	
	137	0.251	2.16×10^{14}	Pb_i^{+}	
	153	0.287	1.82×10^{14}	Pb_i^{2+}	
	176	0.33	1.32×10^{15}	Pb_i^{2+}	
Melt Method (VB)	22.2	0.02821	6.34×10^{12}	Cs_i^{+}	36
	37.5	0.05428	1.53×10^{13}	Pb_{Br}^{+}	
	50.6	**0.07851**	1.48×10^{13}	$\mathbf{V_{Br}^{+}}$	
	59.3	0.09513	5.83×10^{13}	-	
	71.3	0.11911	1.11×10^{14}	-	
	87.3	0.15178	1.07×10^{14}	V_{Cs}^{-}	
	96.8	0.17183	1.28×10^{13}	-	
	117.1	0.21540	3.92×10^{13}	Pb_i^{+}	
	158.2	0.30762	7.70×10^{12}	Pb_i^{+}	
	232.1	0.48175	1.12×10^{13}	Pb_{Br}^{2+}	

Supplementary Note 11: Computational methods

All results of calculations in this work were performed in the framework of the density functional theory (DFT) with the projector augmented plane-wave method, as implemented in the Vienna ab initio simulation package (VASP)[37]. The generalized gradient approximation proposed by Perdew–Burke–Ernzerhof (PBE), is selected for the exchange-correlation potential[38,39]. The cut-off energy for a plane wave is set to 500 eV. The energy criterion is set to 10^{-5} eV in the iterative solution of the Kohn-Sham equation. The Brillouin zone integration is performed using a 2 × 3 × 2 k-mesh. All the structures are relaxed until the residual forces on the atoms have declined to less than 0.02 eV/Å. The energy barriers for Br^- ion diffusion in the structures were computed by the nudged elastic band (CI-NEB) method. The migration path of Br ions vacancies is shown in Supplementary Fig. 33.

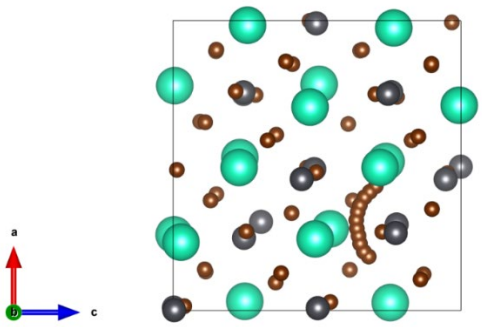

Supplementary Fig. 33 Migration path of Br^- ion vacancies in a $CsPbBr_3$ crystal with Br^- vacancies, and the brown dots represent the migration direction.

Supplementary Note 12: X-ray Detection Instrument and calibration of X-ray dose rates

The X-ray generating and shielding device was fabricated to characterize the X-ray detection capability of the $CsPbBr_3$ SCs detectors. Supplementary Fig. 34a exhibited the photograph of the tungsten anode VAREX RAD-14/Leo X-ray tube (upper part) and the Ralco R302L/A beam limiter (lower part inside the shielding lead box). The EMD EPS SYS 50R high-voltage generator, which provides bias voltages, is beside the shielding lead box (Supplementary Fig. 34b). Moreover, the Keithley 6517b high resistance meter provides bias voltages with the detectors and the computer records data (Supplementary Fig. 34b). Our devices were placed under the X-ray beam limiter without any filters when exposed to the X-ray photon energies of 40, 70, and 120 keV. The X-ray radiation window size of the beam limiter was 1 × 1 spaces for knobs, and the distance between the window and detector was 130 cm.

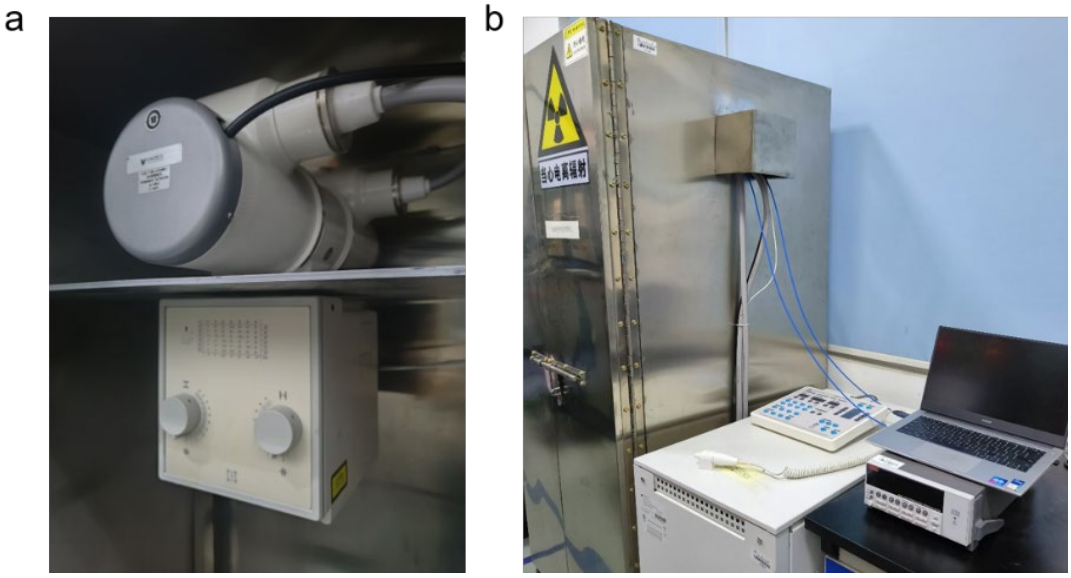

Supplementary Fig. 34 a) The tungsten anode X-ray tube and manual X-ray Collimator inside the shielding lead box. b) The shielding lead box, the high-voltage generator, and the high resistance meter.

The radiation dose rates were calibrated using the Piranha 655 X-ray machine multifunctional quality detector by adjusting the currents of the tube from 10-25 mA, respectively. The calibration results are listed in Supplementary Table 5 for 40, 70, and

120 keV X-ray photons, and the dose rates are calibrated for 120 keV X-rays with a 7 mm-thick standard copper plate inserted between the detector and the X-ray source in Supplementary Table 6.

Supplementary Table 5. Dose rate calibration of 40, 70, and 120 keV X-rays[17].

Tube current (mA)	40 keV Dose rate ($\mu Gy_{air}\ s^{-1}$)	70 keV Dose rate ($\mu Gy_{air}\ s^{-1}$)	120 keV Dose rate ($\mu Gy_{air}\ s^{-1}$)
10	1.13	4.14	12.24
12.5	1.53	5.2	15.25
16	1.91	6.65	19.21
20	2.41	8.42	24.44
25	3.06	10.66	30.74

Supplementary Table 6. Dose rate calibration of 120 keV X-rays with a 7 mm-thick standard copper plate inserted between the detector and the X-ray source.

Tube current (mA)	Dose rate-1 ($nGy_{air}\ s^{-1}$)	Dose rate-2 ($nGy_{air}\ s^{-1}$)	Dose rate-3 ($nGy_{air}\ s^{-1}$)	Average dose rate ($nGy\ s^{-1}$)
10	178	194	182	184.66
12.5	238	242	234	238.00
16	285	289	292	288.66
20	353	365	361	359.66
25	444	460	448	450.66

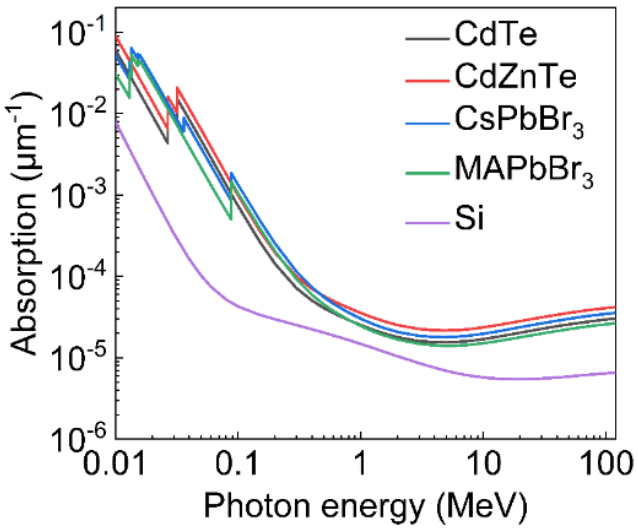

Supplementary Fig. 35 Attenuation coefficients of different materials under the X-ray photon energy from 10-100 MeV.

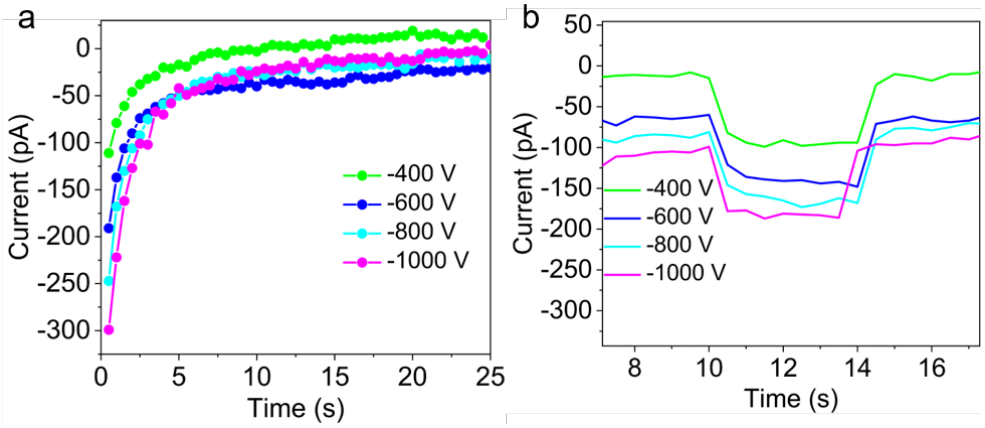

Supplementary Fig. 36 (a) *I-t* curves and (b) responses under 120 keV X-ray irradiation (30.74 $\mu Gy_{air}\ s^{-1}$) for air ionization. The thickness of the device is 2.0 mm, and the maximum bias voltage applied to the device is -1000 V. The air ionization currents were measured by removing the detector and keeping the distance of two probes at 2 mm. In our measurements, the air ionization current (180 pA) is negligible as it is 400 times smaller than the signal current (80 nA) at the same high electric field of 5000 V cm^{-1} (Supplementary Fig. 36). Therefore, we believe that the air ionization current is negligible.

Supplementary Note 13: X-ray responses of the $CsPbBr_3$ SC devices

The sizes of $CsPbBr_3$ SC wafers are 4.0 × 4.0 × 2.0 mm^3. The Au electrode was sputtered on one side of the crystal, and the EGaIn electrode was coated on the other surface of the crystal. The work functions of the EGaIn and the Au electrodes are around 4.2 and 5.1 eV, respectively. The area of the electrodes all are 0.04 cm^{-2}.

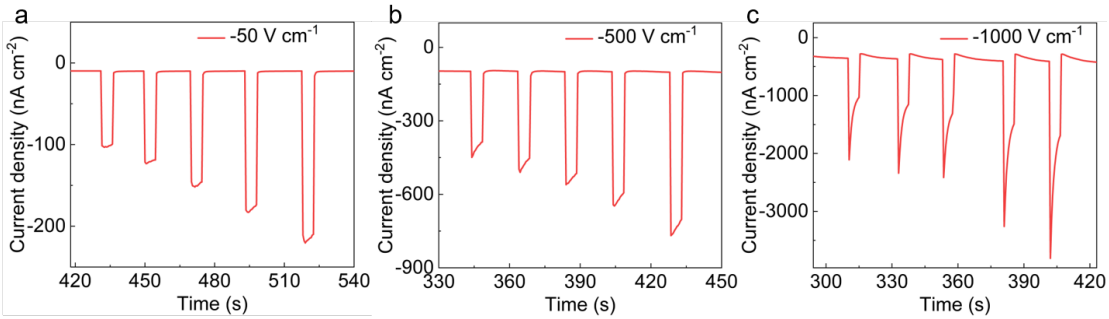

Supplementary Fig. 37 Device responses of the VB-$CsPbBr_3$ SCs-based detectors under electric fields ranged from -50 to -1000 V cm^{-1}. Both the photocurrents and dark currents of the VB-$CsPbBr_3$ detector were stable at negative fields between -50 and -500 V cm^{-1}, but they fluctuated when the electric field reached -1000 V cm^{-1}.

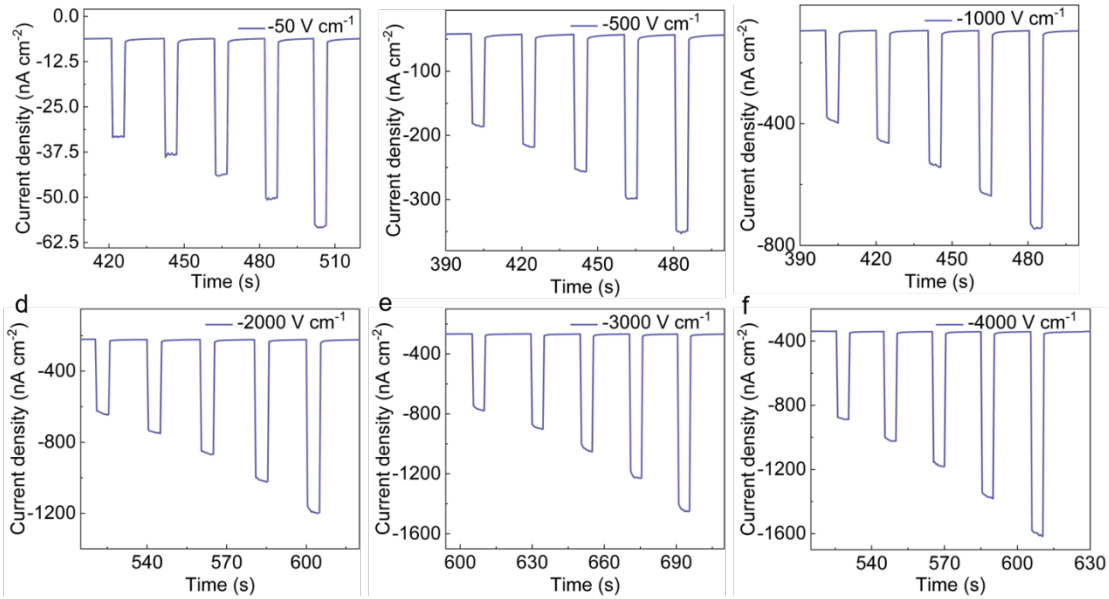

Supplementary Fig. 38 Device responses of the EFG-$CsPbBr_3$ SCs-based detectors under electric fields ranged from -50 to -4000 V cm^{-1}. The current baselines of the EFG-$CsPbBr_3$ SC device are stable under the electric fields from -50 to -4000 V cm^{-1}.

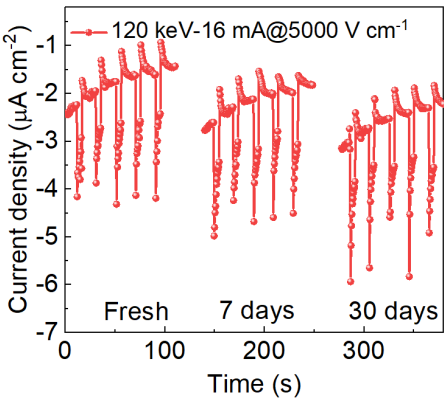

Supplementary Fig. 39 X-ray response stability of the VB-$CsPbBr_3$ SC detector for 120 keV at room conditions.

Supplementary Note 14: X-ray sensitivities of the $CsPbBr_3$ SC devices

The generated current densities were proportional to the X-ray doses under different electric fields, and the X-ray sensitivities were calculated as[3]

$$S = \frac{I_{\text{photo}} - I_{\text{dark}}}{A \cdot R} \tag{13}$$

where I_{photo} and I_{dark} represent the photocurrent and dark current for the device, respectively, R is the X-ray dose, and A is the effective area of the device. The sensitivity of the EFG-$CsPbBr_3$ SC detector under -1000 V cm^{-1} (14693 μC Gy_{air}^{-1} cm^{-2}) was 10 times higher than the Ga/$CsPbBr_3$ film/Au under -1200 V cm^{-1} (1450 μC Gy_{air}^{-1} cm^{-2}) under 70 keV X-rays irradiation

Supplementary Table 7 Sensitivities of the EFG-$CsPbBr_3$ SC detector for 40 keV X-rays under different electric fields.

Electric field (V cm^{-1})	Sensitivities (μC Gy_{air}^{-1} cm^{-2})
-500	3675
-1000	5995
-2000	6824
-3000	8489
-4000	9955
-5000	11991

Supplementary Table 8 Sensitivities of the EFG-$CsPbBr_3$ SC detector for 70 keV X-rays under different electric fields.

Electric field (V cm^{-1})	Sensitivities (μC Gy_{air}^{-1} cm^{-2})
-500	7788
-1000	14693
-2000	20385
-3000	24756
-4000	28696
-5000	32881

Supplementary Table 9 Sensitivities of the EFG-$CsPbBr_3$ SC detector for 120 keV X-rays under different electric fields.

Electric field (V cm^{-1})	Sensitivities (μC Gy_{air}^{-1} cm^{-2})
-500	8748
-1000	18780
-2000	29727
-3000	35936
-4000	41178
-5000	46180

Supplementary note 15: Current drift of the $CsPbBr_3$ SC devices

The current drift D can be expressed as[5]:

$$D = \frac{J_t - J_0}{t \cdot E} \tag{14}$$

where t denotes the duration, E is the electric field, and J_t and J_0 are the current densities at the beginning and ending points, respectively.

Supplementary note 16: Signal-to-noise (SNR) of the $CsPbBr_3$ SC devices

The SNR value of the current response can be calculated as follows[3]:

$$SNR = \frac{I_{photo} - I_{dark}}{\sqrt{\frac{\sum_i^n \left(I_i - I_{photo}\right)^2}{N}}} \quad (15)$$

where I_{photo} denotes the average photocurrent, I_{dark} denotes the average dark current, and I_i denotes the generated photocurrent.

Supplementary note 17: X-ray imaging for the $CsPbBr_3$ SC devices

An EFG-$CsPbBr_3$ SC wafer with dimensions of 11 × 10 mm^2, a thickness of 2 mm, and electrodes measuring 0.5 × 0.5 mm^2 for 15 × 15-pixel arrays is shown in Supplementary Fig. 40a. To evaluate the potential for X-ray imaging of the SC detectors, we scanned a hoop beneath a lid shell with the X-ray beam (Supplementary Fig. 40b). Diverse X-ray energies cause different photocurrents in objects of various densities. As shown in Supplementary Fig. 41, the VB-$CsPbBr_3$ SC device failed to discriminate between the two objects due to its extra low SNRs (2.09 and 1.86 for the hoop and the lid edge, respectively), only revealing the form of the lid (Supplementary Fig. 43). In contrast, the EFG-$CsPbBr_3$ SC device achieved high SNRs of 16.07 and 16.41 for the hoop and the lid edge, respectively, leading to the shape of the hoop and the lid edge appearing in the X-ray image in Supplementary Fig. 42. When the X-ray energy was tuned to 120 keV, the photocurrent response at the plastic lid edge was the same as that of the air due to the large penetration capacity of 120 keV X-ray photons into the lid. Moreover, the edge of the hoop was barely discernible in the X-ray image with a low SNR (9.55) of the VB-$CsPbBr_3$ SC device (Supplementary Figs. 41, 43). However, the whole hoop with the edge was clearly revealed in the X-ray image for the EFG-$CsPbBr_3$ SC device due to the large signal currents and high SNR (24.91) (Supplementary Fig. S42). Consequently, the EFG-$CsPbBr_3$ SC with a small dark current and a high SNR can distinguish the signals generated by the objects of different densities under X-rays of different energies.

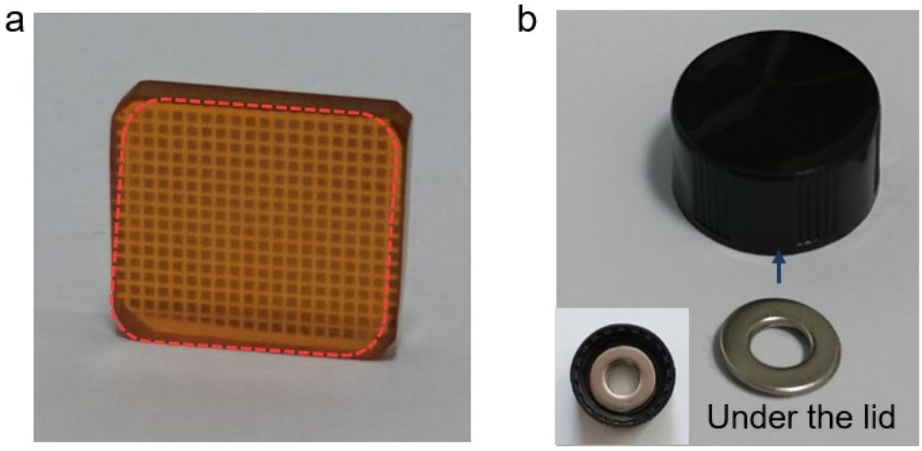

Supplementary Fig. 40 a) Photograph of the EFG-$CsPbBr_3$ SC detector. b) Photograph of a hoop under a lid. The inset shows the photograph of the metal hoop under a plastic lid turned upside down.

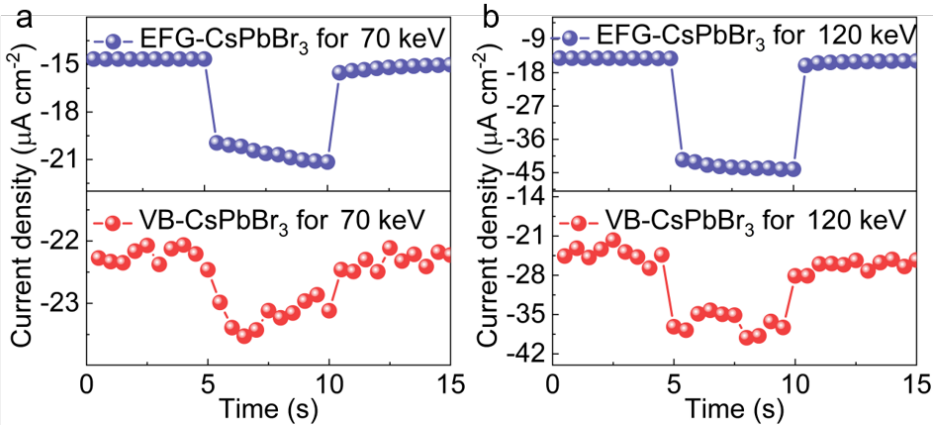

Supplementary Fig. 41 X-ray response to the plastic lid edge of $CsPbBr_3$ SCs detectors for a) 70 and b) 120 keV X-ray photons.

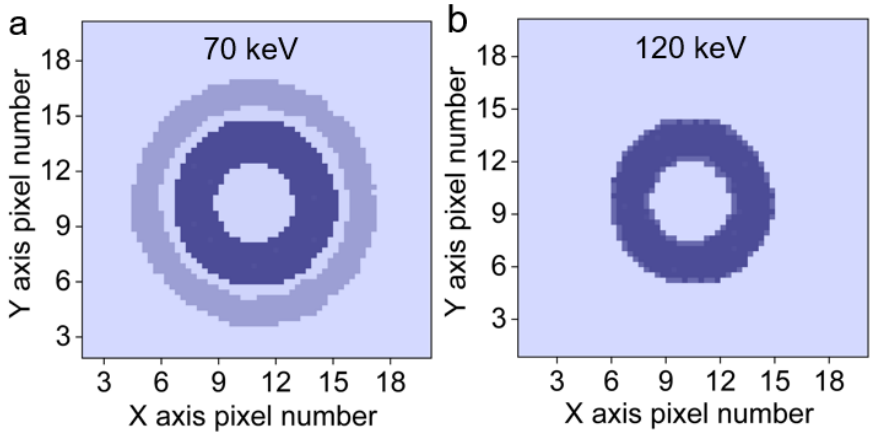

Supplementary Fig. 42 X-ray images of the objects for EFG-$CsPbBr_3$ SCs detector under a) 70 and b) 120 keV X-ray irradiation.

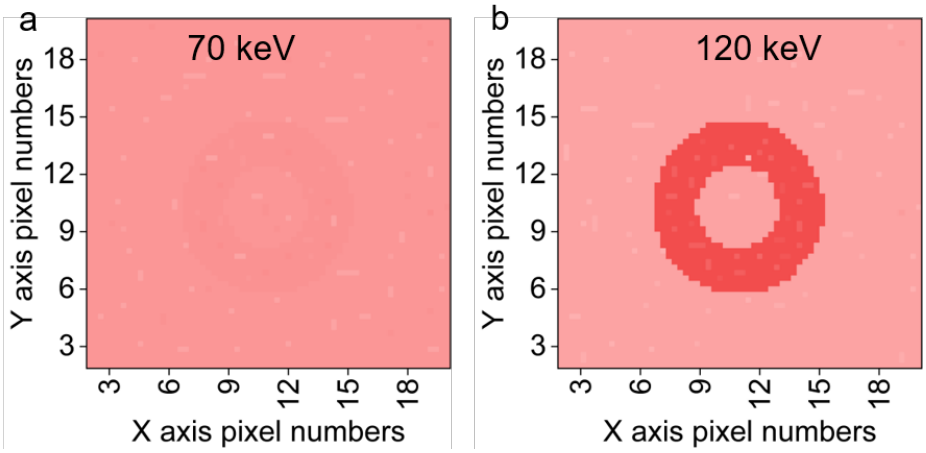

Supplementary Fig. 43 X-ray images of the objects for VB-$CsPbBr_3$ SCs detector under a) 70 and b) 120 keV X-ray irradiation.

References

1 Liu, J. et al. Flexible, Printable Soft-X-Ray Detectors Based on All-Inorganic Perovskite Quantum Dots. *Adv. Mater.* **31**, e1901644 (2019).

2 Wei, H. et al. Dopant compensation in alloyed $CH_3NH_3PbBr_{3-x}Cl_x$ perovskite single crystals for gamma-ray spectroscopy. *Nat. Mater.* **16**, 826-833 (2017).

3 Pan, W. et al. $Cs_2AgBiBr_6$ single-crystal X-ray detectors with a low detection limit. *Nat. Photon.* **11**, 726-732 (2017).

4 Ma, C. et al. Centimeter-Sized 2D Perovskitoid Single Crystals for Efficient X-ray Photoresponsivity. *Chem. Mater.* **34**, 1699-1709 (2022).

5 Xia, M. et al. Unveiling the Structural Descriptor of $A_3B_2X_9$ Perovskite Derivatives toward X-Ray Detectors with Low Detection Limit and High Stability. *Adv. Funct.Mater.* **30**, 1910648 (2020).

6 Tie, S. et al. Robust Fabrication of Hybrid Lead-Free Perovskite Pellets for Stable X-ray Detectors with Low Detection Limit. *Adv. Mater.* **32**, 2001981 (2020).

7 Liu, Y. et al. Triple-Cation and Mixed-Halide Perovskite Single Crystal for High-Performance X-ray Imaging. *Adv. Mater.* **33**, 2006010 (2021).

8 Song, Y. et al. Atomistic Surface Passivation of $CH_3NH_3PbI_3$ Perovskite Single Crystals for Highly Sensitive Coplanar-Structure X-Ray Detectors. *Research* **2020**, 5958243 (2020).

9 Zhang, B. et al. High-Performance X-ray Detection Based on One-Dimensional Inorganic Halide Perovskite $CsPbI_3$. *J. Phys. Chem. Lett.* **11**, 432-437 (2020).

10 He, Y. et al. Sensitivity and Detection Limit of Spectroscopic-Grade Perovskite $CsPbBr_3$ Crystal for Hard X-Ray Detection. *Adv. Funct. Mater.* **32**, 2112925 (2022).

11 Jiang, J. et al. Synergistic strain engineering of perovskite single crystals for highly stable and sensitive X-ray detectors with low-bias imaging and monitoring. *Nat. Photon.* **16**, 575-581 (2022).

12 Matt, G. J. et al. Sensitive Direct Converting X-Ray Detectors Utilizing Crystalline $CsPbBr_3$ Perovskite Films Fabricated via Scalable Melt Processing. *Adv. Mater. Interfaces* **7**, 1901575 (2020).

13 Geng, X. et al. High-performance single crystal $CH_3NH_3PbI_3$ perovskite x-ray detector. *Appl. Phys. Lett.* **118**, 40653 (2021).

14 Li, X. et al. Dimensional and Optoelectronic Tuning of Lead-free Perovskite $Cs_3Bi_2I_{9-n}Br_n$ Single Crystals for Enhanced Hard X-ray Detection. *Angew. Chem. Int. Ed.* **62**, e202315817 (2023).

15 Kim, Y. C. et al. Printable organometallic perovskite enables large-area, low-dose X-ray imaging. *Nature* **550**, 87-91 (2017).

16 Zheng, X. et al. Ultrasensitive and stable X-ray detection using zero-dimensional lead-free perovskites. *J. Energy Chem.* **49**, 299-306 (2020).

17 Zhang, P. et al. Ultrasensitive and Robust 120 keV Hard X-Ray Imaging Detector based on Mixed-Halide Perovskite $CsPbBr_{3-n}I_n$ Single Crystals. *Adv. Mater.* **34**, e2106562 (2022).

18 Li, W. et al. Fine-control-valve of halide perovskite single crystal quality for high performance X-ray detection. *Sci. Bull.* **66**, 2199-2206 (2021).

19 Li, H. et al. Sensitive and Stable 2D Perovskite Single-Crystal X-ray Detectors Enabled by a Supramolecular Anchor. *Adv. Mater.* **32**,202003790 (2020).

20 Katyba, G. M. et al. Sapphire Photonic Crystal Waveguides for Terahertz Sensing in Aggressive Environments. *Adv. Opt. Mater.* **6**, 1800573 (2018).

21 Masuya, S. et al. Characterization of crystalline defects in β-Ga_2O_3 single crystals grown by edge-defined film-fed growth and halide vapor-phase epitaxy using synchrotron X-ray topography. *Jap. J. Appl. Phys.* **58**, 055501 (2019).

22 Guguschev, C. et al. The application of floating dies for high speed growth of CsI single crystals by edge-defined film-fed growth (EFG). *J. Cryst. Growth* **404**, 231-240 (2014).

23 Ghorui, C. et al. Comparative studies of terahertz-based optical properties in transmission/reflection modes of GaSe: S and measurement of its scattering losses due to surface roughness for efficient terahertz generation. *Phys. Scr.* **98**, 025508 (2023)

24 Chen, X. et al. Temperature Dependent Reflectance and Ellipsometry Studies on a $CsPbBr_3$ Single Crystal. *J. Phys. Chem. C* **123**, 10564-10570 (2019).

25 Wang, Y. et al. Direct Radiation Detection by a Semiconductive Metal-Organic Framework. *J. Am. Chem. Soc.* **141**, 8030-8034 (2019).

26 Zhang, H. et al. High-sensitivity X-ray detectors based on solution-grown caesium lead bromide single crystals. *J. Mater. Chem. C* **8**, 1248-1256 (2020).

27 Dong S. et al. Low trap-state density and long carrier diffusion in organolead trihalide perovskite single crystals. *Science* **347**, 519-522 (2015).

28 Duijnstee, E. A. et al. Toward Understanding Space-Charge Limited Current Measurements on Metal Halide Perovskites. *ACS Energy Lett.* **5**, 376-384 (2020).

29 Li, Y. et al. Shallow traps-induced ultra-long lifetime of metal halide perovskites probed with light-biased time-resolved microwave conductivity. *Appl. Phys. Rev.* **10**, 129883 (2023).

30 Jia, Z. et al. Charge-Carrier Dynamics of Solution-Processed Antimony- and Bismuth-Based Chalcogenide Thin Films. *ACS Energy Lett.* **8**, 1485-1492 (2023).

31 Afroz, M. A. et al. Impedance Spectroscopy for Metal Halide Perovskite Single Crystals: Recent Advances, Challenges, and Solutions. *ACS Energy Lett.* **6**, 3275-3286 (2021).

32 Mahapatra, A. et al. Reducing ion migration in methylammonium lead tri-bromide single crystal via lead sulfate passivation. *J. Appl. Phys.* **127**, 185501 (2020).

33 García-Batlle, M. et al. Moving Ions Vary Electronic Conductivity in Lead Bromide Perovskite Single Crystals through Dynamic Doping. *Adv. Electron. Mater.* **6**, 2000485 (2020).

34 Zhang, B. et al. Defect proliferation in $CsPbBr_3$ crystal induced by ion migration. *Appl. Phys. Lett.* **116**, 063505 (2020).

35 Wang, F. et al. Precursor Engineering for Solution Method-Grown Spectroscopy-Grade $CsPbBr_3$ Crystals with High Energy Resolution. *Chem. Mater.* **34**, 3993-4000 (2022).

36 Zhang, M. et al. Determination of Defect Levels in Melt-Grown All-Inorganic Perovskite $CsPbBr_3$ Crystals by Thermally Stimulated Current Spectra. *J. Phys. Chem. C* **122**, 10309-10315 (2018).

37 Perdew, J. P., Burke, K., Ernzerhof, M. Generalized Gradient Approximation Made Simple. *Phys. Rev. Lett*. **77**, 3865 (1996).

38 Xiao, R. et al. High-throughput design and optimization of fast lithium ion conductors by the combination of bond-valence method and density functional theory. *Sci. Rep.* **5**, 14227 (2015).

39 Yang, B. et al. Heteroepitaxial passivation of $Cs_2AgBiBr_6$ wafers with suppressed ionic migration for X-ray imaging. *Nat. Commun.* **10**, 1989 (2019).